Room-Temperature Preparation, Characterization, and Photoluminescence Measurements of Solid Solutions of Various Compositionally-Defined Single-Crystalline Alkaline-Earth-Metal Tungstate Nanorods

Fen Zhang,[†] Matthew Y. Sfeir,[‡] James A. Misewich,[‡] and Stanislaus S. Wong*,[†,‡]

Department of Chemistry, State University of New York at Stony Brook, Stony Brook, New York 11794-3400 and Condensed Matter Physics and Materials Sciences Department, Brookhaven National Laboratory, Building 480, Upton, New York 11973

Received January 2, 2008. Revised Manuscript Received June 4, 2008

The current report describes the systematic synthesis of single-crystalline alkaline-earth-metal tungstate AWO_4 (A = Ca, Sr, Ba) nanorods as well as a series of their crystalline solid−solution analogues $Sr_{1-x}Ca_xWO_4$ and $Ba_{1-x}Sr_xWO_4$ ($0 < x < 1$) with controllable chemical composition and morphology using a modified template-directed methodology under ambient room-temperature conditions. Extensive characterization of the resulting nanorods has been performed using diffraction, X-ray photoelectron spectroscopy, electron microscopy, and optical spectroscopy. The composition-modulated luminescence properties of these alkaline-earth-metal tungstate solid−solution nanorods provide for a fundamental understanding of the intrinsic optical and optoelectronic properties of these systems, suggesting, therefore, the possibility of their rational incorporation into functional nanoscale devices.

Introduction

Alkaline-earth-metal tungstates AWO_4 (A = Ca, Sr, Ba) represent an important family of inorganic, electrooptic materials[1–3] with their distinctive scheelite structure and associated highly interesting physical properties such as excitonic luminescence, thermoluminescence, and stimulated Raman scattering (SRS). In fact, they are keenly sought as host materials for a wide range of technologically significant applications,[4–17] including as phosphors, gas sensors, laser media, and optical fibers as well as components of electrochromic devices, amplifiers, diagnostic medical equipment, microwave systems, and the next generation of scintillator detectors. In the scheelite structure, the tungsten ions adopt a tetrahedral coordination within oxygen-ion cages and are isolated from each other while the relatively large bivalent cations (i.e., Ca, Sr, and Ba with ionic radii > 0.99 Å) are surrounded by eight oxygen ions (Figure S1).[18,19]

One key point is that all of the as-mentioned applications, which render scheelites as appropriately attractive materials, are evidently and intimately coupled with their lattice dimension, crystallographic symmetry, as well as band structure. Hence, in this article, we seek to gain a fundamental understanding of how slight but controlled variations in the chemical composition of these scheelite materials may lead to favorable structure−property correlations in these systems.

One viable and legitimate experimental strategy for approaching this problem lies in the reproducible and reliable generation of stoichiometrically controlled, homogeneous, single-phase solid solutions of such materials. For example, by rationally altering the precursor compositions of ZnS and $AgInS_2$, the energy gap of highly luminescent $(AgIn)_xZn_{(1-x)}S_2$ solid solution nanoparticles could be modulated through

* To whom correspondence should be addressed. Phone: 631-632-1703. 631-344-3178. E-mail: sswong@notes.cc.sunysb.edu; sswong@bnl.gov.
[†] State University of New York at Stony Brook.
[‡] Brookhaven National Laboratory.

(1) Saito, N.; Sonoyama, N.; Sakata, T. *Bull. Chem. Soc. Jpn.* **1996**, *69*, 2191.
(2) Liao, H.-W.; Wang, Y.-F.; Liu, X.-M.; Li, Y.-D.; Qian, Y.-T. *Chem. Mater.* **2000**, *12*, 2819.
(3) Kloprogge, J. T.; Weier, M. L.; Duong, L. V.; Frost, R. L. *Mater. Chem. Phys.* **2004**, *88*, 438.
(4) Wang, H.; Medina, F. D.; Zhou, Y. D.; Zhang, Q. N. *Phys. Rev. B* **1992**, *45*, 10356.
(5) Nagirnyi, V.; Feldbach, E.; Jönsson, L.; Kirm, M.; Lushchik, A.; Lushchik, C.; Nagornaya, L. L.; Ryzhikov, V. D.; Savikhin, F.; Svensson, G.; Tupitsina, I. A. *Radiat. Mes.* **1998**, *29*, 247.
(6) Park, I.-H.; Kim, B.-S.; Kim, K.-Y.; Kim, B.-H. *Jpn. J. Appl. Phys.* **2001**, *40*, 4956.
(7) Li, L.; Su, Y.; Li, G. *Appl. Phys. Lett.* **2007**, *90*, 054105.
(8) Zhang, Q.; Yao, W.-T.; Chen, X.; Zhu, L.; Fu, Y.; Zhang, G.; Sheng, L.; Yu, S.-H. *Cryst. Growth Des.* **2007**, *7*, 1423.
(9) Nitsch, K.; Nikl, M.; Ganschow, S.; Reiche, P.; Uecker, R. *J. Cryst. Growth* **1996**, *165*, 163.
(10) Kaminskii, A. A.; Eichler, H. J.; Ueda, K.-I.; Klassen, N. V.; Redkin, B. S.; Li, L. E.; Findeisen, J.; Jaque, D.; García-Sole, J.; Fernández, J.; Balda, R. *Appl. Opt.* **1999**, *38*, 4533.
(11) Treadaway, M. J.; Powell, R. C. *Phys. Rev. B* **1975**, *11*, 862.
(12) Martini, M.; Meinardi, F.; Spinolo, G.; Vedda, A. M. N.; Usuki, Y. *Phys. Rev. B* **1999**, *60*, 4653.
(13) Cho, W.-S.; Yashima, M.; Kakihana, M.; Kudo, A.; Sakata, T.; Yoshimura, M. *Appl. Phys. Lett.* **1995**, *66*, 1027.
(14) Yu, S.-H.; Liu, B.; Mo, M.-S.; Huang, J.-H.; Liu, X.-M.; Qian, Y.-T. *Adv. Funct. Mater.* **2003**, *13*, 639.
(15) Pode, R. B.; Dhoble, S. J. *Phys. Status Solidi B* **1997**, *203*, 571.
(16) Kobayashi, M.; Usukib, Y.; Ishiic, M.; Yazawac, T.; Harad, K.; Tanakad, M.; Nikle, M.; Nitsch, K. *Nucl. Instrum. Methods Phys. Res. A* **1997**, *399*, 261.
(17) Murk, V.; Nikl, M.; Mihokova, E.; Nitsch, K. *J. Phys.: Condens. Matter* **1997**, *9*, 249.
(18) Errandonea, D.; Somayazulu, M.; Häusermann, D. *Phys. Status Solidi B* **2003**, *235*, 162.
(19) Sun, L.; Guo, Q.; Wu, X.; Luo, S.; Pan, W.; Huang, K.; Lu, J.; Ren, L.; Cao, M.; Hu, C. *J. Phys. Chem. C* **2007**, *111*, 532.

10.1021/cm800011j CCC: $40.75 © 2008 American Chemical Society
Published on Web 08/06/2008

a wide range of visible light, thereby enabling tuning of the emission color of these materials from green to red, depending on their chemical composition; this nanoscale chemical manipulation had implications for the photocatalytic behavior of these systems.[20–22] In another case, the degree of ferromagnetism, magnetoresistance, and transport behavior of epitaxial $Cr_xTi_{1-x}N$ thin films grown using pulsed laser deposition were found to depend very strongly on the magnitude of x.[23] Moreover, the conductivity and dielectric properties of $Ba_{5x/2}Bi_{(1-x)5/3}Nb_5O_{15}$[24] and $YBa_{1-x}Sr_xCo_2O_{5+\delta}$,[25] respectively, were observed to vary with chemical composition, degree of oxygen ordering, as well as the nature of the cation substitution. In addition, it has been demonstrated that solid solutions of $Zn_xTi_{1-x}O_{2-x}$ evince significant photocatalytic activity in the photodegradation of phenols.[26] Theoretically, it has been shown that the hardness parameter as well as elastic constants associated with multicomponent solid solutions of nitride spinels, titanium nitrogen carbides (e.g., $TiN_{1-x}C_x$), transition-metal nitrides (e.g., TiN_{1-x}), and B-doped semiconductors (e.g., Si_xB_{1-x}) as well as of $U_xLa_{1-x}S$ systematically depend on predictive adjustment of x.[27,28] Of particular pertinence to this work, it has been demonstrated that unlike for scheelite-powellite solid solutions,[29] the family of pure scheelite-type metal tungstates allows for isomorphic replacement of the divalent metal cation, thereby creating a highly miscible solid solution over vast compositional ranges.[30–32]

The second key point, i.e., the equally important, motivating factor for the current work, resides in the development of low-dimensional nanomaterials with controllable size, shape, and morphology for realization of novel functional devices at the nanoscale.[33–35] In particular, one-dimensional (1D) nanostructures, including nanowires, nanorods, nanobelts, and nanotubes, are the focus of intensive research owing to their unique, shape-dependent properties, allowing for their use as building blocks in the assembly of a range of electronic, optoelectronic, and sensing devices.[36–38] Part of the challenge in this area is the rational and precise tuning of the chemical composition of these 1D structures so as to systematically optimize their optical, mechanical, and electronic properties. The most popular strategies for reliable 1D nanostructure preparation involve kinetic control of growth provided by capping reagents,[39,40] formation from a confined alloy droplet, as described by a vapor−liquid−solid (VLS) growth mechanism,[41,42] generation using a chimie douce solution method,[43,44] and, finally, synthesis using template-directed methodologies.[45,46]

In terms of previous work with nanoscale alkaline-earth-metal tungstates, the vast majority of prior results have focused on generation of either nanoparticles or nanoparticle aggregates,[7,8,47–49] synthesized using either hydrothermal, solvothermal, or molten salt methodologies. Nonetheless, work on creating one-dimensional nanostructures of these scheelite materials does exist. For example, $CaWO_4$ nanorods, with widths of about 20 nm and lengths of 100−250 nm, have been fabricated using a solvothermal technique in the presence of PEG-200 at 180 °C and at pH 9 for 14 h;[50] slightly longer nanorods with average diameters of 20−30 nm and mean lengths of 600−1000 nm were controllably generated using a microemulsion-mediated hydrothermal procedure.[51] With respect to $SrWO_4$, nanorods measuring 100 nm in diameter and 500−1500 nm in length were synthesized using a solvothermal-mediated microemulsion technique involving water, organic solvent, and surfactant.[19] For $BaWO_4$ nanorods, their 2-dimensional organization at the water−air interface was accomplished using a Langmuir−Blodgett technique.[52,53] Recently, uniform, high-aspect-ratio, single-crystalline $BaWO_4$ nanorods with diameters as small as 3.5 nm and lengths up to more than 50 μm were synthesized using a catanionic reversed micelle templating protocol;[54,55] bundles of these nanorods could be generated

(20) Tsuji, I.; Kato, H.; Kobayashi, H.; Kudo, A. *J. Am. Chem. Soc.* **2004**, *126*, 13406.
(21) Torimoto, T.; Adachi, T.; Okazaki, K.; Sakuraoka, M.; Shibayama, T.; Ohtani, B.; Kudo, A.; Kuwabata, S. *J. Am. Chem. Soc.* **2007**, *129*, 12388.
(22) Tsuji, I.; Kato, H.; Kudo, A. *Chem. Mater.* **2006**, *18*, 1969.
(23) Inumaru, K.; Koyama, K.; Miyaki, Y.; Tanaka, K.; Yamanaka, S. *Appl. Phys. Lett.* **2007**, *91*, 152501.
(24) Muktha, B.; Simon, A.; Darriet, J.; Guru Row, T. N. *Chem. Mater.* **2006**, *18*, 1240.
(25) McKinlay, A.; Connor, P.; Irvine, J. T. S.; Zhou, W. *J. Phys. Chem. C* **2007**, *111*, 19120.
(26) Kolen'ko, Y. V.; Kovnir, K. A.; Gavrilov, A. I.; Garshev, A. V.; Meskin, P. E.; Churagulov, B. R.; Bouchard, M.; Colbeau-Justin, C.; Lebedev, O. I.; Van Tendeloo, G.; Yoshimura, M. *J. Phys. Chem. B* **2005**, *109*, 20303.
(27) Hu, Q. M.; Kádas, K.; Hogmark, S.; Yang, R.; Johansson, B.; Vitos, L. *Appl. Phys. Lett.* **2007**, *91*, 121918.
(28) Varshney, D.; Kaurav, N.; Kinge, R.; Singh, R. K. *J. Phys.: Condens. Matter* **2007**, *19*, 346212.
(29) Fernandez-Gonzalez, A.; Andara, A. P. M. *Cryst. Growth Des.* **2007**, *7*, 545.
(30) Liegeois-Duyckaerts, N.; Tarte, P. *Spectrochim. Acta, Part A* **1972**, *28*, 2037.
(31) Cho, W.-S.; Yashima, M.; Kakihana, M.; Kudo, A.; Sakata, T.; Yoshimura, M. *Appl. Phys. Lett.* **1996**, *68*, 137.
(32) Cho, W.-S.; Yoshimura, M. *Jpn. J. Appl. Phys.* **1997**, *36*, 5658.
(33) Wang, Z. L.; Song, J. *Science* **2006**, *312*, 242.
(34) Ge, J.; Hu, Y.; Yin, Y. *Angew. Chem., Int. Ed.* **2007**, *46*, 7428.
(35) Kovalenko, M. V.; Bodnarchuk, M. I.; Lechner, R. T.; Hesser, G.; Schäffler, F.; Heiss, W. *J. Am. Chem. Soc.* **2007**, *129*, 6352.
(36) Xia, Y.; Yang, P.; Sun, Y.; Wu, Y.; Mayers, B.; Gates, B.; Yin, Y.; Kim, F.; Yan, H. *Adv. Mater.* **2003**, *15*, 353.
(37) Rutherglen, C.; Burke, P. *Nano Lett.* **2007**, *7*, 3296.
(38) Ma, R.-M.; Dai, L.; Huo, H.-B.; Xu, W.-J.; Qin, G. G. *Nano Lett.* **2007**, *7*, 3300.
(39) Puntes, V. F.; Krishnan, K. M.; Alivisatos, A. P. *Science* **2001**, *291*, 2115.
(40) Yu, C.; Varghese, L.; Irudayaraj, J. *Langmuir* **2007**, *23*, 9114.
(41) Hu, J.; Odom, T. W.; Lieber, C. M. *Acc. Chem. Res.* **1999**, *32*, 435.
(42) Kodambaka, S.; Tersoff, J.; Reuter, M. C.; Ross, F. M. *Science* **2007**, *316*, 729.
(43) Zhang, G.; Zhang, T.; Lu, X.; Wang, W.; Qu, J.; Li, X. *J. Phys. Chem. C* **2007**, *111*, 12663.
(44) Lan, W.-J.; Yu, S.-H.; Qian, H.-S.; Wan, Y. *Langmuir* **2007**, *23*, 3409.
(45) Chattopadhyay, S.; Shi, S. C.; Lan, Z. H.; Chen, C. F.; Chen, K.-H.; Chen, L.-C. *J. Am. Chem. Soc.* **2005**, *127*, 2820.
(46) Zhang, G.; Lu, X.; Zhang, T.; Qu, J.; Wang, W.; Li, X.; Yu, S. *Nanotechnology* **2006**, *17*, 4252.
(47) Su, Y.; Li, G.; Xue, Y.; Li, L. *J. Phys. Chem. C* **2007**, *111*, 6684.
(48) Wang, Y.; Ma, J.; Tao, J.; Zhu, X.; Zhou, J.; Zhao, Z.; Xie, L.; Tian, H. *Mater. Lett.* **2006**, *60*, 291.
(49) Li, D.; Wu, H.; Li, Z.; Cong, X.; Sun, J.; Ren, Z.; Liu, L.; Li, Y.; Fan, D.; Hao, J. *Colloids Surf. A* **2006**, *274*, 18.
(50) Chen, S.-J.; Li, J.; Chen, X.-T.; Hong, J.-M.; Xue, Z.; You, X.-Z. *J. Cryst. Growth* **2003**, *253*, 361.
(51) Sun, L.; Cao, M.; Wang, Y.; Sun, G.; Hu, C. *J. Cryst. Growth* **2006**, *289*, 231.
(52) Kwan, S.; Kim, F.; Akana, J.; Yang, P. *Chem. Commun.* **2001**, *447*.
(53) Kim, F.; Kwan, S.; Akana, J.; Yang, P. *J. Am. Chem. Soc.* **2001**, *123*, 4360.
(54) Shi, H.; Qi, L.; Ma, J.; Cheng, H. *Chem. Commun.* **2002**, *1704*.

in combination with a solvothermal methodology.[56] With the further use of double-hydrophilic block copolymers as effective crystal growth modifiers, morphological variants, namely, penniform $BaWO_4$ nanostructures, could be prepared using this generalized reverse micellar technique.[57]

Nonetheless, development of facile, mild (i.e., under ambient conditions), and effective approaches for creating size-controlled, chemically precise, and crystalline 1D alkaline-earth-metal tungstate nanostructures as well as their associated array architectures remains a significant scientific challenge, especially because control of chemical composition in these systems would lead to a correspondingly high degree of predictability in the photoluminescence properties of these systems.[31,58] Resolving this issue is the convergence point of the two key interests outlined in this paper. That is, we performed the synthesis and optical characterization of a series of stoichiometrically controlled, homogeneous, single-phase solid solutions of 1D nanomaterials in order to deduce systematic, nanoscale structure−property correlations. Specifically, the interactions between the calcium, strontium, and barium ions and the emission centers in discrete solid solutions of these oxide nanomaterials may contribute differentially to their observed optical spectra.

To accomplish this overall goal, whereas conventional templating procedures typically generate polycrystalline products as a result of the necessity of additional annealing steps at high temperature,[36] we recently developed a modified template-directed technique. This protocol has allowed us to previously prepare pure single-crystalline metal oxide and fluoride nanorods under ambient conditions while utilizing reasonably stable and nontoxic precursors in aqueous solution and without generating large quantities of harmful byproducts.[59–61] Specifically, in this article, we report on the successful generalization of this synthetic protocol to preparation of not only 1D nanostructures of an entire family of alkaline-earth-metal tungstate scheelite structures but also their single-crystalline, stoichiometrically defined solid−solution analogues with controllable size and chemical composition. Experimentally, a commercially available, track-etched polycarbonate membrane of varying pore size was mounted between two halves of a U-shaped reaction tube, each of which contained aqueous precursor solutions, so as to control the growth of the corresponding 1D nanostructures. As a rigorous and logical extension of our previous work on $BaWO_4$ nanorods,[60] herein we not only decreased the diameters of as-prepared barium tungstate nanostructures to 50 nm but also extended this generalizable methodology to the preparation of calcium tungstate and strontium tungstate analogues. Moreover, we systematically characterized the luminescence properties of several series of samples prepared within a wide range of tunable, achievable chemical compositions and found a linear correlation between optical behavior and tungstate stoichiometry. In addition, we measured lifetimes and quantum yields associated with our systems.

Experimental Section

Synthesis. Polycarbonate (PC) track-etch membranes of ca. 6 μm thickness, containing pore sizes of 50, 100, and 200 nm diameter, were purchased from Whatman Co., U.K. The membranes were initially hydrated by immersion and sonication in a small volume of distilled, deionized water for a few minutes so as to limit air bubble formation either within their interior pore structures or on their external surfaces. In order to avoid unwanted particle formation and deposition onto the exterior sides of the PC templates, microcontact-printed OTS-SAMs (octadecyltetrachlorosilane self-assembled monolayers) were used as passivation layers on the external surfaces of the PC membranes.[62] As such, a homemade PDMS (polydimethylsiloxane) stamp was initially inked with a 10 mM hexane solution of OTS and dried with nitrogen. The stamp was then placed into contact with the PC membranes for 30 s and later carefully peeled off.

Subsequently, the polymer membrane was mounted between two half arms of a U-shaped tube cell. In a typical synthesis, one of the two half cells was filled with Na_2WO_4 solution and the other half cell contained a solution of either $CaCl_2$, $SrCl_2$, or $Ba(NO_3)_2$ to correspondingly generate $CaWO_4$, $SrWO_4$, or $BaWO_4$ nanorods, respectively. Solid−solution $Sr_{1-x}Ca_xWO_4$ and $Ba_{1-x}Sr_xWO_4$ nanorods, respectively, were prepared by mixing relevant molar ratios of either $CaCl_2$ and $SrCl_2$ or $SrCl_2$ and $Ba(NO)_3$ solutions, respectively, depending on the desired nanostructure, into the appropriate U-tube half cell containing the metal ions. The system was then left unperturbed for an incubation period of up to 1 day at room temperature. Subsequent to immersion, the polycarbonate membrane was detached, sonicated for about 2 min to remove unwanted particles on the surface, and thoroughly washed with distilled water prior to being dissolved in methylene chloride solution. As-prepared tungstate nanorods were collected from solution by centrifugation after washing.

As a typical protocol for functionalizing nanorods with capping ligands, 5 mg of as-prepared $CaWO_4$ nanorods was dispersed in 10 mL of distilled, deionized water and subsequently stirred with 0.5 g/L of either poly(acrylic acid) (PAA) or sodium oleate for 1 day. Isolated nanorod precipitates were cleaned by washing multiple times with distilled, deionized water.

Characterization. To prepare powder X-ray diffraction (XRD) samples, the resulting tungstate nanorods were rendered into slurries in ethanol, sonicated for about 1 min, and then air dried upon deposition onto glass slides. Multiple, replicate diffraction patterns were collected using a Scintag diffractometer, operating in the Bragg configuration using Cu Kα radiation ($\lambda = 1.54$ Å) from 10° to 80° at a scanning rate of 2°/min.

For X-ray photoelectron spectroscopy (XPS) analyses, pressed sample wafers were attached onto stainless steel holders using conductive double-sided tape and installed in the vacuum chamber of a model DS DS800 XPS surface analysis system (Kratos Analytical Plc of Manchester, U.K.). The chamber was evacuated to a base pressure of $\sim 5 \times 10^{-9}$ Torr. A hemispherical energy analyzer was used for electron detection. XPS spectra were then collected using a Mg Kα X-ray source at an 80 eV pass energy

(55) Shi, H.; Qi, L.; Ma, J.; Cheng, H.; Zhu, B. *Adv. Mater.* **2003**, *15*, 1647.
(56) Zhang, C.; Shen, E.; Wang, E.; Kang, Z.; Gao, L.; Hu, C.; Xu, L. *Mater. Chem. Phys.* **2006**, *96*, 240.
(57) Shi, H.; Qi, L.; Ma, J.; Cheng, H. *J. Am. Chem. Soc.* **2003**, *125*, 3450.
(58) Cho, W.-S.; Yoshimura, M. *J. Am. Ceram. Soc.* **1996**, *79*, 2783.
(59) Mao, Y.; Park, T. J.; Zhang, F.; Zhou, H.; Wong, S. S. *Small* **2007**, *3*, 1122.
(60) Mao, Y.; Wong, S. S. *J. Am. Chem. Soc.* **2004**, *126*, 15245.
(61) (a) Mao, Y.; Zhang, F.; Wong; S. S. *Adv. Mater.* **2006**, *18*, 1895; (b) Zhang, F.; Mao, Y.; Park, T. J.; Wong; S. S. *Adv. Funct. Mater.* **2006**, *18*(1), 103
(62) Kumar, A.; Whitesides, G. M. *Appl. Phys. Lett.* **1993**, *63*, 2002.

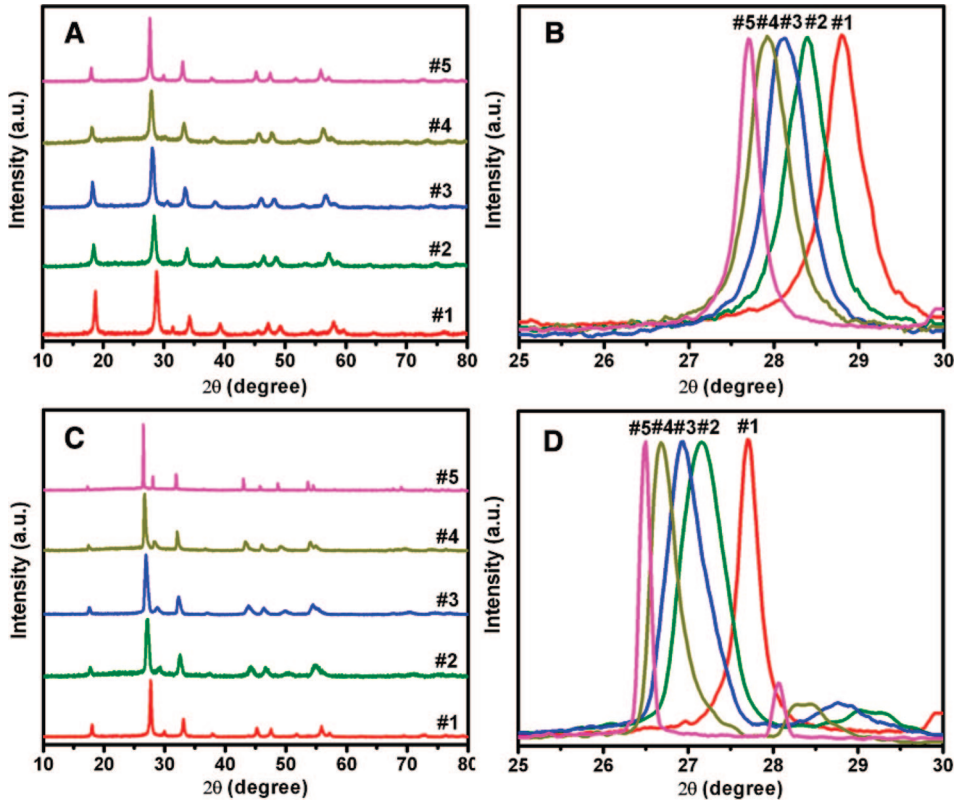

Figure 1. (A) XRD patterns of as-prepared $Sr_{1-x}Ca_xWO_4$ nanorod samples in the 2θ range of 10−80°: (1) $CaWO_4$, (2) $Sr_{0.3}Ca_{0.7}WO_4$, (3) $Sr_{0.5}Ca_{0.5}WO_4$, (4) $Sr_{0.7}Ca_{0.3}WO_4$, and (5) $SrWO_4$. Labels and colors are identical for B. (B) Expanded view of the 2θ diffraction peaks between 25° and 30° for all five of the $Sr_{1-x}Ca_xWO_4$ nanorod samples. (C) XRD patterns of as-prepared $Ba_{1-x}Sr_xWO_4$ nanorod samples in the 2θ range of 10−80°: (1) $SrWO_4$, (2) $Ba_{0.3}Sr_{0.7}WO_4$, (3) $Ba_{0.5}Sr_{0.5}WO_4$, (4) $Ba_{0.7}Sr_{0.3}WO_4$, and (5) $BaWO_4$. Labels and colors are identical for D. (D) Expanded view of the 2θ diffraction peaks between 25° and 30° for all five of the $Ba_{1-x}Sr_xWO_4$ nanorod samples.

and in 0.75 eV steps for each sample survey spectrum. High-resolution spectra were collected for the major elements detected in order to study the nature of the chemical bonding in these materials. These spectra were obtained at a pass energy of 40 eV and in 0.1 eV steps.

The diameters and lengths of as-prepared nanorods were initially characterized using a field emission scanning electron microscopy instrument (FE-SEM Leo 1550), operating at an accelerating voltage of 15 kV and equipped with energy-dispersive X-ray spectroscopy (EDS) capabilities. Samples for scanning electron microscopy (SEM) were prepared by dispersing as-prepared tungstate nanorods in ethanol, sonicating for about 2 min, and then depositing the sample onto either a conductive tape or a silicon wafer, attached to a SEM brass stub. All of these samples were then conductively coated with gold by sputtering for 15 s to minimize charging effects under SEM imaging conditions. Low-magnification transmission (TEM) images were taken at an accelerating voltage of 80 kV on a FEI Tecnai12 BioTwinG^2 instrument equipped with an AMT XR-60 CCD Digital Camera System. High-resolution TEM (HRTEM) images and selected area electron diffraction (SAED) patterns were obtained on a JEOL 2010F instrument at accelerating voltages of 200 kV. Specimens for all of these TEM experiments were prepared by dispersing the as-prepared product in ethanol, sonicating for 2 min to ensure adequate dispersion of the nanorods, and dipping one drop of the solution onto a 300 mesh Cu grid, coated with a lacey carbon film.

Midinfrared spectra were obtained on a Nexus 670 (Thermo Nicolet) equipped with a single-reflectance ZnSe ATR accessory, a KBr beam splitter, and a DTGS KBr detector. As-prepared solid powder samples were placed onto a ZnSe crystal, where data were taken with a reproducible pressure. A background correction was performed using the ZnSe crystal in the spectral range studied.

Samples for photoluminescence (PL) spectra were dispersed in deionized water and sonicated for 1 min to obtain a finely dispersed particulate suspension of approximately 1 mg/mL of nanorods in solution. To test the effect of length distribution on these optical properties, as-prepared nanorods were sonicated for 1 h to obtain correspondingly shorter, fragmented structures. Fluorescence data were subsequently obtained at room temperature on a Jobin Yvon Spex Fluorolog 3 with a 10 s integration time using an excitation wavelength of 350 nm.

Time-resolved emission spectra were measured at room temperature using a Varian Cary-Eclipse fluorescence spectrometer. The excitation wavelength used for our lifetime measurements was 190 nm as it yielded the strongest luminescence signals. Spectra were measured at 502 nm with a 2 μs gate time.

Results and Discussion

X-ray Diffraction. The purity and crystallinity of the two series of as-prepared $Sr_{1-x}Ca_xWO_4$ and $Ba_{1-x}Sr_xWO_4$ ($0 \leq x \leq 1$) nanorods were initially characterized using powder X-ray diffraction (XRD). Figure 1A shows diffraction patterns collected from five $Sr_{1-x}Ca_xWO_4$ samples of varying compositions in the 2θ range of 10−80°. Very little if any elemental impurity peaks were noted. All of the diffraction peaks for Sample 1 in Figure 1A can be readily indexed to the pure body-centered tetragonal phase [space group $I4_1/a$] of $CaWO_4$, with calculated lattice constants of $a = 5.240 \pm 0.011$ Å and $c = 11.371 \pm 0.016$ Å, which are in good agreement with the literature values of the corresponding bulk counterpart ($a = 5.242$ Å, $c = 11.372$ Å, JCPDS File No. 07-0210). Similarly, diffraction peaks for Sample 5 in

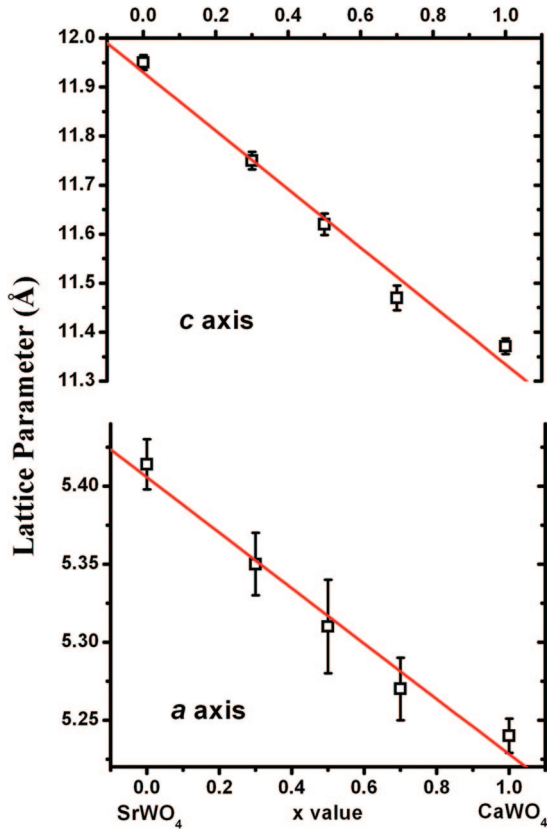

Figure 2. Systematic variation of the lattice parameters associated with $Sr_{1-x}Ca_xWO_4$ nanorods as a function of solid−solution composition.

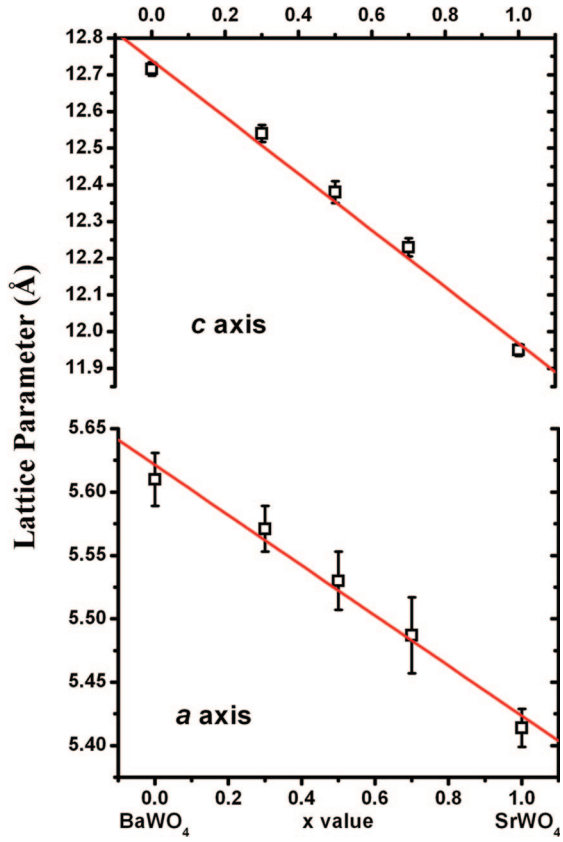

Figure 3. Systematic variation of the lattice parameters associated with $Ba_{1-x}Sr_xWO_4$ nanorods as a function of solid−solution composition.

Figure 1A can be ascribed to a pure body-centered tetragonal phase [space group $I4_1/a$] of $SrWO_4$ with accompanying lattice constants of $a = 5.414 \pm 0.016$ Å and $c = 11.950 \pm 0.015$ Å, which are comparable in value to the corresponding reported data of $a = 5.417$ Å and $c = 11.951$ Å (JCPDS File No. 08-0490) for the bulk.

When we more carefully analyzed all five XRD patterns in Figure 1A simultaneously, we generally observed that each peak for $Sr_{1-x}Ca_xWO_4$ nanorods shifted to a lower 2θ value with increasing Sr concentration. For example, Figure 1B illustrates XRD peak behavior at 2θ values between 25° and 30° for all five samples. It can be clearly observed that the (112) peak initially corresponding to the tetragonal phase of $CaWO_4$ gradually shifts to lower 2θ positions as a function of composition, eventually transforming into the (112) peak of the tetragonal phase of $SrWO_4$. The exact (112) peak 2θ positions for the five samples were located at 28.80°, 28.38°, 28.08°, 27.96°, and 27.70°, corresponding to nanorod compositions of $CaWO_4$, $Sr_{0.3}Ca_{0.7}WO_4$, $Sr_{0.5}Ca_{0.5}WO_4$, $Sr_{0.7}Ca_{0.3}WO_4$, and $SrWO_4$, respectively. Calculated unit-cell lattice parameters, namely, **a** and **c**, assuming tetragonal $Sr_{1-x}Ca_xWO_4$, varied effectively monotonically with composition change, as shown in Figure 2 and in agreement with Vegard's law, described as follows in eqs 1 and 2

$$\mathbf{a}(Sr_{1-x}Ca_xWO_4) = \mathbf{a}(CaWO_4) + (1-x)[\mathbf{a}(SrWO_4) - \mathbf{a}(CaWO_4)] \quad (1)$$

$$\mathbf{c}(Sr_{1-x}Ca_xWO_4) = \mathbf{c}(CaWO_4) + (1-x)[\mathbf{c}(SrWO_4) - \mathbf{c}(CaWO_4)] \quad (2)$$

Our results are consistent with a previously observed data sequence for a continuous compositional range of $Sr_{1-x}Ca_xWO_4$ films. It should be noted that neither an apparent phase separation nor a separate nucleation of either $CaWO_4$ or $SrWO_4$ was observed in the alloyed solid-state solutions.[31]

By analogy, X-ray diffraction patterns of $Ba_{1-x}Sr_xWO_4$ ($0 \leq x \leq 1$) nanorods are shown in Figure 1C. All of the diffraction peaks for each of the samples shifted to lower 2θ positions upon increasing the Ba concentration. Unit-cell parameters for $Ba_{1-x}Sr_xWO_4$ changed continuously from $a = 5.414 \pm 0.016$ Å and $c = 11.950 \pm 0.015$ Å for tetragonal $SrWO_4$ ($x = 1$) to $a = 5.610 \pm 0.021$ Å and $c = 12.716 \pm 0.018$ Å for tetragonal $BaWO_4$ ($x = 0$). These unit-cell values correlate well with reported database numbers for the corresponding pure tungstates (i.e., JCPDS File Nos. 08-0490 and 08-0457), respectively. Figure 1D shows the behavior of the (112) peak, corresponding to the tetragonal phase of $Ba_{1-x}Sr_xWO_4$ in greater detail. When the value of x changes systematically from 1 to 0, the peak positions shifted continuously from 27.70° to 26.48° with decreasing Sr concentration in each of the five samples. Calculated unit-cell lattice parameters, assuming tetragonal $Ba_{1-x}Sr_xWO_4$, varied essentially monotonically with systematic composition change, as shown in Figure 3 and in agreement with Vegard's law, described as follows in eqs 3 and 4

$$\mathbf{a}(Ba_{1-x}Sr_xWO_4) = \mathbf{a}(SrWO_4) + (1-x)[\mathbf{a}(BaWO_4) - \mathbf{a}(SrWO_4)] \quad (3)$$

$$\mathbf{c}(Ba_{1-x}Sr_xWO_4) = \mathbf{c}(SrWO_4) + (1-x)[\mathbf{c}(BaWO_4) - \mathbf{c}(SrWO_4)] \quad (4)$$

Our results are consistent with a previously observed data sequence for a continuous compositional range of electrochemically prepared $Ba_{1-x}Sr_xWO_4$ solid−solution films.[32] By

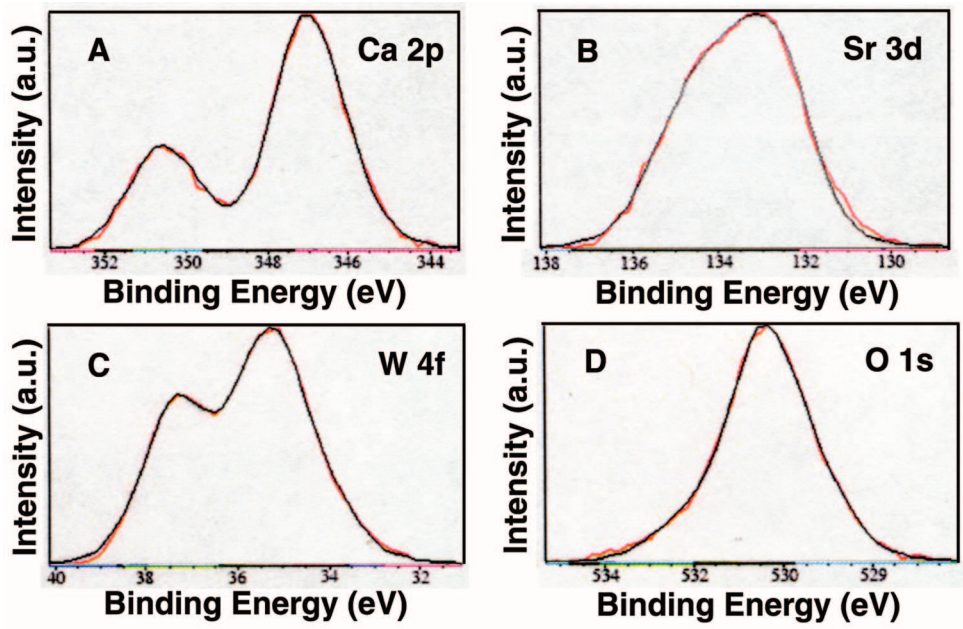

Figure 4. XPS spectra of as-prepared $Sr_{0.3}Ca_{0.7}WO_4$ nanorod samples: (A) Ca 2p spectrum, (B) Sr 3d spectrum, (C) W 4f spectrum, and (D) O 1s spectrum.

analogy, neither a noted phase separation nor a separate nucleation of either $BaWO_4$ or $SrWO_4$ was apparent for these alloyed solid-state solution samples.

X-ray Photoelectron Spectroscopy. The survey X-ray photoelectron spectroscopy (XPS) spectra collected on successive $Sr_{1-x}Ca_xWO_4$ nanorod samples (where $x = 0.7$, 0.5, 0.3) are shown in Figure S2. Peak values localized at 34.8, 132.4, 530.1, and 346.9 eV can be readily assigned to the binding energies of W 4f, Sr 3d, O 1s, and Ca 2p, respectively. It is evident that the amount of Sr gradually decreases while that of Ca systematically increases with increasing x values in this series of samples. By XPS, the atomic ratio of Ca:Sr content was found to vary from 2.5:1, 1.1:1, and finally to 0.46:1 as the molar value of x was systematically altered from 0.7, 0.5, to 0.3 in the precursor solutions. These experimental data are in acceptable agreement with the calculated atomic ratios of Ca:Sr, which theoretically ought to have altered from 2.3:1, 1:1, and ultimately to 0.43:1 with the corresponding variation in solid−solution composition.

Figure 4 shows typical high-resolution XPS spectra of as-prepared $Sr_{0.3}Ca_{0.7}WO_4$ nanorod samples. The Ca 2p peaks and Sr 3d peak (Figure 4A and 4B) are consistent with the oxidation states of Ca and Sr, as both being +2, respectively, which also supports the notion that Ca ions can be randomly substituted by Sr ions within the scheelite structure.[31] Moreover, the W 4f and O 1s spectra (Figure 4C and 4D) are consistent with oxidation states of W^{6+} and O^{2-}, respectively, which would be expected from the anticipated formation of WO_4^{2-} groups in these nanoscale samples.[63] Similar high-resolution XPS spectra have been obtained for as-prepared $Sr_{0.5}Ca_{0.5}WO_4$ and $Sr_{0.7}Ca_{0.3}WO_4$ nanorod samples (Figure S3 and S4).

Survey XPS spectra collected on $Ba_{0.3}Sr_{0.7}WO_4$ and $Ba_{0.5}Sr_{0.5}WO_4$ nanorod samples (Figure S5) also highlight the systematic variation of Sr and Ba content with corresponding changes in the magnitude of x values. By XPS, the atomic ratio of Sr: Ba content was found to vary from 2.7:1 and 1.3:1 for $Ba_{0.3}Sr_{0.7}WO_4$ and $Ba_{0.5}Sr_{0.5}WO_4$ nanorod solid solutions, respectively. These experimental data are in reasonable agreement with the calculated atomic ratios of Sr:Ba, which theoretically ought to have altered from 2.3:1 to 1:1 with the corresponding variation in solid solution composition. Moreover, detailed information on the intrinsic nature of the chemical bonding in these systems was collected using high-resolution XPS spectra, as shown in Figures 5 and S6. The Sr 3d and Ba 3d peaks (Figure 5A and 5B), located at 132.4 and 779.5 eV for $Ba_{0.3}Sr_{0.7}WO_4$ nanorods, are consistent with the oxidation states of Ba and Sr, as both being +2, respectively, which also supports the notion that Ba ions can be randomly substituted by Sr ions within the scheelite structure.[64] Figure 5C and 5D further confirm the existence of WO_4^{2-} groups in these nanorod samples.

Electron Microscopy. Figure 6 shows SEM images and the corresponding EDS data of all five as-prepared $Sr_{1-x}Ca_xWO_4$ (where $x = 1$, 0.7, 0.5, 0.3, and 0) nanorod samples, which were fabricated using polycarbonate membranes with pore sizes as small as 50 nm. It can be observed that all the products of (A) $CaWO_4$, (B) $Sr_{0.3}Ca_{0.7}WO_4$, (C) $Sr_{0.5}Ca_{0.5}WO_4$, (D) $Sr_{0.7}Ca_{0.3}WO_4$, and (E) $SrWO_4$ mainly consist of straight and smooth nanorods with uniform, homogeneous size along their axis direction. By analyzing magnified SEM images of these five samples, as shown in the insets of Figure 6A−E, diameters of the wire-like nanorods obtained were noted to be in the range of 50 ± 5 nm, based on the corresponding as-reported 50 nm pore sizes of the commercial templates used in the synthesis. Measured lengths

(63) Atuchin, V. V.; Kesler, V. G.; Maklakova, N. Y.; Pokrovsky, L. D.; Sheglov, D. V. *Eur. Phys. J. B* **2006**, *51*, 293.

(64) Itoh, M.; Fujita, N.; Inabe, Y. *J. Phys. Soc. Jpn.* **2006**, *75*, 084705.

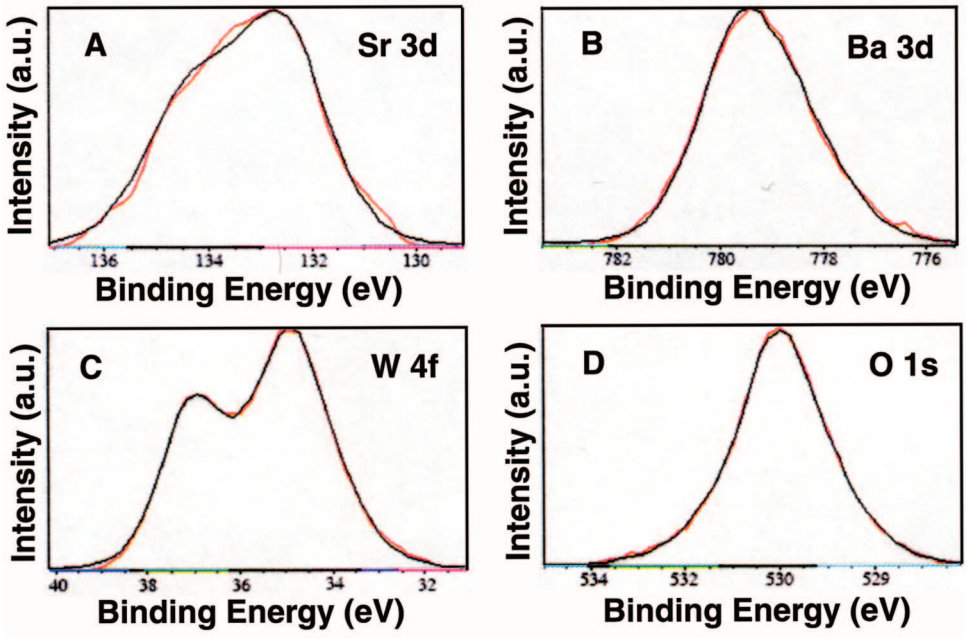

Figure 5. XPS spectra of as-prepared $Ba_{0.3}Sr_{0.7}WO_4$ nanorod samples: (A) Sr 3d spectrum, (B) Ba 3d spectrum, (C) W 4f spectrum, and (D) O 1s spectrum.

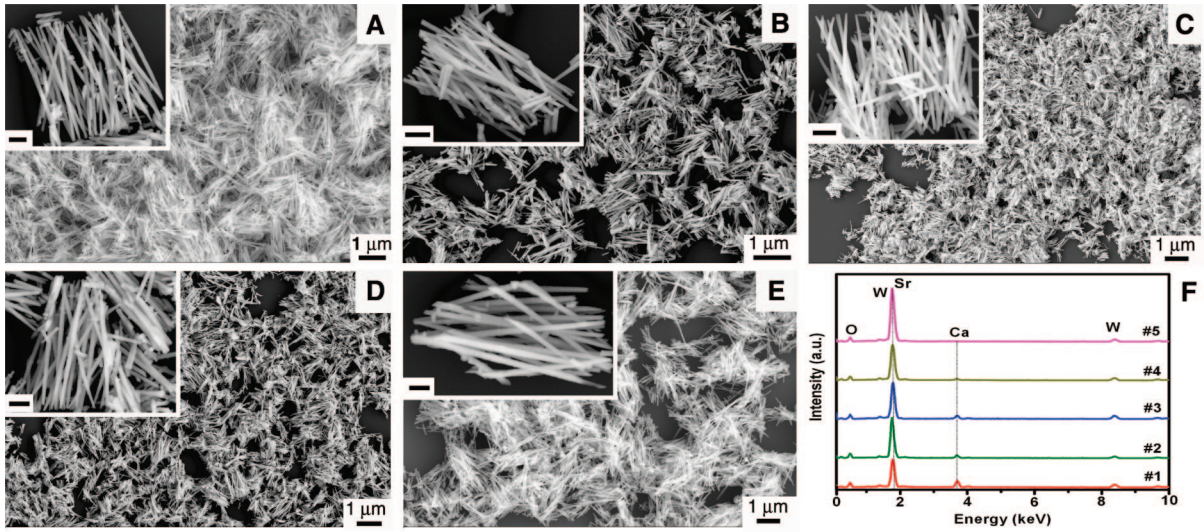

Figure 6. Representative SEM images of as-prepared $Sr_{1-x}Ca_xWO_4$ nanorod samples generated using polycarbonate membranes composed of 50-nm pore sizes: (A) $CaWO_4$, (B) $Sr_{0.3}Ca_{0.7}WO_4$, (C) $Sr_{0.5}Ca_{0.5}WO_4$, (D) $Sr_{0.7}Ca_{0.3}WO_4$, and (E) $SrWO_4$. Associated insets show corresponding magnified views of the as-generated products. Scale bars in the insets are 200 nm. (F) EDS spectra of all five of the $Sr_{1-x}Ca_xWO_4$ nanorods: (1) $CaWO_4$, (2) $Sr_{0.3}Ca_{0.7}WO_4$, (3) $Sr_{0.5}Ca_{0.5}WO_4$, (4) $Sr_{0.7}Ca_{0.3}WO_4$, and (5) $SrWO_4$. Intensities of the peaks for each of the samples have been normalized based on the intensity of the second W peak.

of the five $Sr_{1-x}Ca_xWO_4$ nanorods varied from one to several micrometers with an average value of 2.8 μm, somewhat shorter than the entire thickness of the membrane, which measures about 6 μm. One possible explanation is that longitudinal nanorod growth is limited to some extent by the availability and accessibility of precursor ions. That is, this parameter is determined not only by the overall reaction time but also by the growth rate of the nanorod diameter across the width of the template pores; at a certain point, the increasing nanorod diameter may become sufficiently large to physically block access to ion diffusion through the membrane. In addition, we should note that the sonication step involved in SEM sample preparation may also have physically shortened some of the nanorods. It is noteworthy that the SEM images were obtained from randomly selected areas of all of the five samples and as such are representative of the overall sizes and shapes of as-prepared $Sr_{1-x}Ca_xWO_4$ nanorods. It is reasonable to conclude that the ultimate morphology of each product accurately replicated the internal pore structure and morphology of the originating polycarbonate membranes and that this factor was independent of the chemical composition of the corresponding $Sr_{1-x}Ca_xWO_4$ solid solutions.

Moreover, in every $Sr_{1-x}Ca_xWO_4$ nanorod sample analyzed by EDS (Figure 6F), chemical signatures taken within different parts of each of the samples were noted to be identical within experimental accuracy, and all of the as-

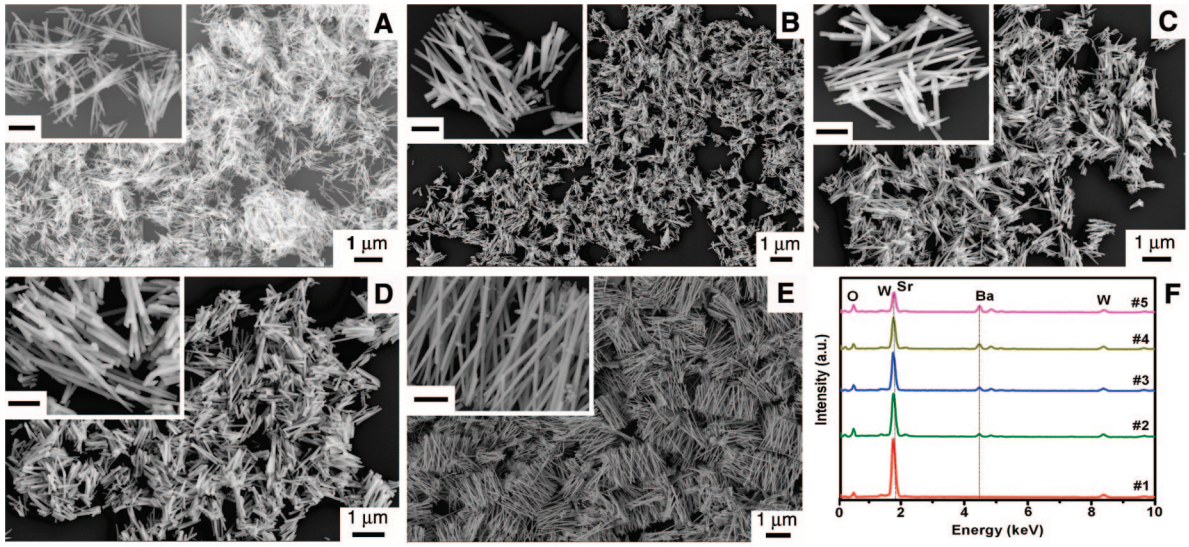

Figure 7. Typical SEM images of as-prepared $Ba_{1-x}Sr_xWO_4$ nanorod samples generated using polycarbonate membranes composed of 100-nm pore sizes: (A) $SrWO_4$, (B) $Ba_{0.3}Sr_{0.7}WO_4$, (C) $Ba_{0.5}Sr_{0.5}WO_4$, (D) $Ba_{0.7}Sr_{0.3}WO_4$, and (E) $BaWO_4$. Associated insets show corresponding magnified views of the as-generated products. Scale bars in the insets are 200 nm. (F) EDS spectra of all five of the $Ba_{1-x}Sr_xWO_4$ nanorods: (1) $SrWO_4$, (2) $Ba_{0.3}Sr_{0.7}WO_4$, (3) $Ba_{0.5}Sr_{0.5}WO_4$, (4) $Ba_{0.7}Sr_{0.3}WO_4$, and (5) $BaWO_4$. Intensities of the peaks for each of the samples have been normalized based on the intensity of the second W peak.

prepared nanorods were essentially composed of elements such as Ca and/or Sr, W, and O, as expected. The Sr signals overlapped with W signals in the energy scale at around 1.9 keV. In the normalized data, the intensities of the Ca signals gradually decrease with either increasing Sr content or decreasing values of x in the $Sr_{1-x}Ca_xWO_4$ system. The actual overall atomic content of Ca for each sample varied from 16.7%, 11.5%, 9.1%, 5.5%, to 0%, corresponding to molar values of $x = 1$, 0.7, 0.5, 0.3, and 0. On the basis of calculation, the theoretical content of Ca in the corresponding sample systems would have been expected to alter from 16.7%, 11.7%, 8.3%, 5.0%, to 0%, respectively, which is in reasonable agreement with experiment. Moreover, this result is consistent with our previously described XPS spectral observations, reinforcing the notion that the chemical compositions of the product $Sr_{1-x}Ca_xWO_4$ nanorod solid solutions are primarily dictated by the initial chemical concentrations of the precursor solutions.

Analogous SEM and EDS data for the as-synthesized $Ba_{1-x}Sr_xWO_4$ system are shown in Figure 7. The microscopy images (Figure 7A–E) showed the presence of dispersed individual nanorods as well as of bundled, aggregated species. In particular, Figure 7E highlights $BaWO_4$ nanorod arrays, where the nanorods are roughly parallel to each other so as to form an aggregate of arrays. All of the straight and crystalline $Ba_{1-x}Sr_xWO_4$ nanorods in Figure 7A−E possessed diameters ranging from 90 to 112 nm and lengths spanning from 2.5 to 5 μm. These nanorods maintained a uniform diameter of around 100 nm throughout their entire length, corresponding to the as-reported 100 nm pore size of the commercial polycarbonate membranes used as templates. Surfaces of these one-dimensional nanostructures were found to be relatively smooth over most of their lengths. EDS spectra (Figure 7F) were taken at a number of selected positions along all five of the $Ba_{1-x}Sr_xWO_4$ samples. Elemental signatures obtained were found to be identical within experimental accuracy, and essentially only Sr and/or Ba, W, and O were detected, as expected. Moreover, it was determined from these data that the peak intensity, representing the atomic content of Ba, increased from 0%, 4.6%, 8.3%, 10.7%, to 15.2% as the value of x decreased from 1, 0.7, 0.5, 0.3, to 0 in the $Ba_{1-x}Sr_xWO_4$ system. Our calculations show that Ba content should have altered from 0%, 5.0%, 8.3%, 11.7%, to 16.7% with a systematic decrease in x over the same range of chemical composition in this solid−solution system, which agrees favorably with our actual results. In addition, our data corroborate previously described XPS measurements, suggesting that the resultant chemical compositions of $Ba_{1-x}Sr_xWO_4$ nanorod solid solutions are mainly determined by the initial chemical concentrations of the precursor solutions.

To provide additional details into the nature of the morphology and crystallographic structure of the $Sr_{1-x}Ca_xWO_4$ and $Ba_{1-x}Sr_xWO_4$ solid−solution systems, as-prepared metal oxide nanorod samples were further analyzed by both low- and high-magnification TEM as well as with selected area electron diffraction (SAED).

Figure 8 shows representative TEM, HRTEM, and SAED images of as-prepared $Sr_{1-x}Ca_xWO_4$ solid−solution nanorods. It can be observed that all the products, prepared using the 50 nm pore size of the polycarbonate membranes, mainly consist of discrete, one-dimensional wire-like nanostructures with smooth outer surfaces and that the as-measured diameters were essentially around 50 nm over much of their lengths. Though these nanorods tended to aggregate fairly easily, as can be seen from their SEM images (Figure 6), a further sonication step could readily resolve this problem and generate isolated nanostructures, as shown in the accompanying TEM images.

All of the HRTEM images and SAED patterns taken along a number of selected regions along each of the individual nanorods were effectively indistinguishable within experimental accuracy for every $Sr_{1-x}Ca_xWO_4$ solid−solution

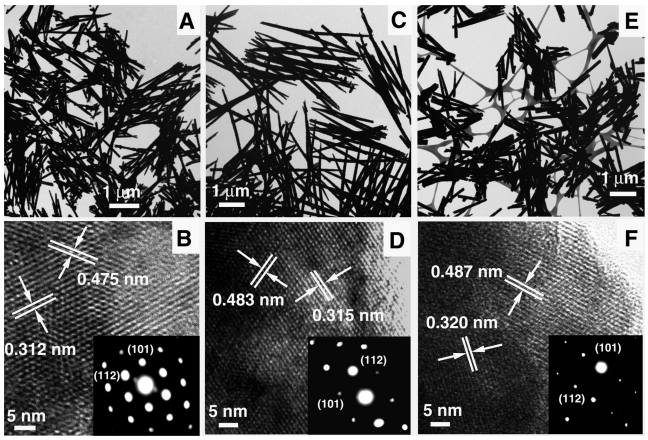

Figure 8. Typical TEM images of as-prepared $Sr_{1-x}Ca_xWO_4$ nanorods using polycarbonate membranes composed of 50-nm pore sizes. HRTEM images of representative portions of individual nanorods. Corresponding SAED patterns are shown in the insets: (A, B) $CaWO_4$; (C, D) $Sr_{0.3}Ca_{0.7}WO_4$; (E, F) $Sr_{0.7}Ca_{0.3}WO_4$.

sample analyzed. A representative HRTEM image taken from a portion of a randomly chosen single $CaWO_4$ nanorod is shown in Figure 8B. The presence of visible, two-dimensional (2D) lattice fringes clearly illustrate that the nanorod is single crystalline with little if any defects or dislocations. Interplanar spacings were computed to be about 3.12 and 4.75 Å, which corresponds to the (112) and (101) planes, respectively. The associated electron diffraction pattern shown in the inset can be indexed to the reflection of a pure body-centered tetragonal $CaWO_4$ scheelite structure. The presence of sharp diffraction spots, as opposed to an amorphous ring, further confirms formation of single-crystalline $CaWO_4$ nanorods, whereas conventional template methods typically yield polycrystalline nanostructures.[36] The corresponding structural analyses from HRTEM data and SAED patterns of as-prepared $Sr_{0.3}Ca_{0.7}WO_4$ and $Sr_{0.7}Ca_{0.3}WO_4$ nanorods, measuring 50 nm in diameter, are presented in Figure 8D and 8F, respectively. By analogy, the presence of clearly visible 2D lattice fringes as well as sharp diffraction spots strongly supports generation of single-crystalline nanorods via our modified template-directed method at room temperature and under ambient conditions. In addition, the interplanar spacings, corresponding to the (112) and (101) planes, respectively, are in good agreement with prior observations noted from the XRD patterns for these materials, corresponding to the tetragonal phase of the scheelite structure.

Similarly, the corresponding TEM images and SAED patterns of the as-prepared $Ba_{1-x}Sr_xWO_4$ solid−solution system, shown in Figure 9, confirm the preparation of single-crystalline $Ba_{1-x}Sr_xWO_4$ nanorods with lattice spacing data consistent with complementary observations generated from XRD data. Indeed, the interplanar spacings, which can be ascribed to the (112) and (101) planes, respectively, tended to increase with decreasing values of x or decreasing Sr content in the $Ba_{1-x}Sr_xWO_4$ system. As can be seen from Figure 9B, 9D, and 9F, the lattice spacings, corresponding to the (112) and (101) planes, increase from 3.24, 3.33, to 3.65 Å and also from 4.95, 5.07, to 5.18 Å, respectively, for the $SrWO_4$, $Ba_{0.7}Sr_{0.3}WO_4$, and $BaWO_4$ nanorod samples. These findings are consistent with the XRD peak behavior we previously detailed as a function of chemical composition

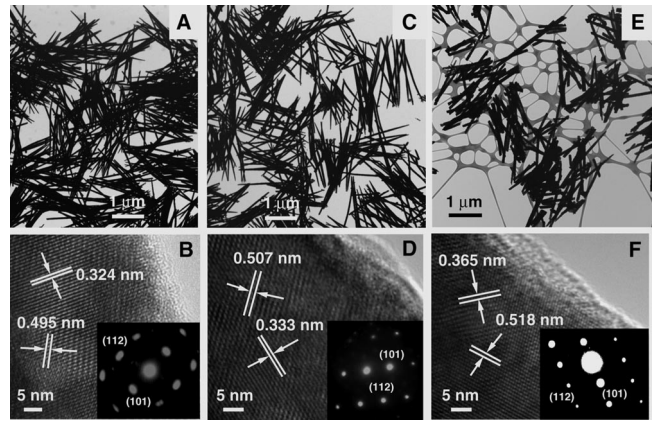

Figure 9. Typical TEM images of as-prepared $Ba_{1-x}Sr_xWO_4$ nanorods using polycarbonate membranes composed of 50-nm pore sizes. HRTEM images of representative portions of individual nanorods. Corresponding SAED patterns are shown in the insets: (A, B) $SrWO_4$; (C, D) $Ba_{0.5}Sr_{0.5}WO_4$; (E, F) $BaWO_4$.

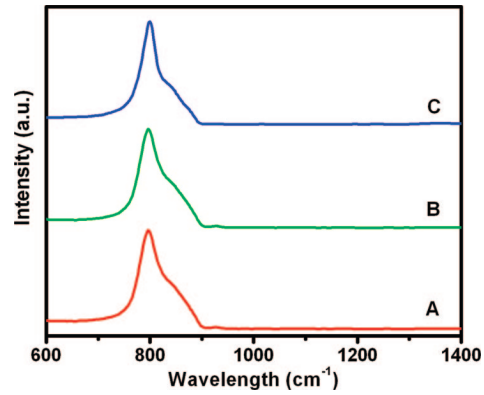

Figure 10. FT-IR spectra of as-prepared single-crystalline alkaline-earth-metal tungstate nanorods: (A) $CaWO_4$; (B) $SrWO_4$; (C) $BaWO_4$.

(Figure 1C and 1D; Figure 3). The same trend was also detected in the $Sr_{1-x}Ca_xWO_4$ solid−solution system in Figure 8, where lattice spacings appeared to increase with decreasing Ca content. Specifically, for the (112) and (101) planes, lattice spacings increased from 3.12, 3.15, to 3.20 Å as well as from 4.75, 4.83, to 4.87 Å for the $CaWO_4$, $Sr_{0.3}Ca_{0.7}WO_4$, and $Sr_{0.7}Ca_{0.3}WO_4$ nanorod samples, respectively. Overall, these results agreed well with the corresponding behavior of the relevant transitions in the associated XRD peaks (Figure 1A and 1B; Figure 2).

Optical Spectroscopy. The optical properties of the as-prepared alkaline-earth-metal tungstate, AWO_4 (A = Ca, Sr, Ba), nanorods were investigated. Figure 10 shows the FT-IR spectra of $CaWO_4$, $SrWO_4$, and $BaWO_4$ nanorods generated using the 50, 100, or 200 nm pore sizes of the polycarbonate membranes, respectively. The strong absorption band located around 800 cm^{-1} appears in Figure 10A of $CaWO_4$ nanorods and likely originates from the W−O antisymmetric stretching vibrational mode, corresponding to the internal υ_3 (B_g) mode in bulk AWO_4-type scheelite oxides.[30,65–67] The presence of similar characteristic absorption bands in Figure 10B and 10C further corroborates the identity of our other as-prepared nanorods as belonging to $SrWO_4$ and $BaWO_4$, respectively, as expected.

As previously mentioned, the emission spectra of scheelite tungstates exhibit a broad luminescence band in the blue spectral region. The as-observed excitonic luminescence can

be attributed to a radiative transition within the undisturbed, anionic, tetrahedral WO_4^{2-} complex.[68–71] The photoluminescence behavior of as-prepared nanorods with different diameters (50, 100, or 200 nm) was noted to be similar, showing little discernible diameter dependence. In another series of experiments, we also found out that PL measurements are not dependent on the length distribution of the nanorods either. Specifically, we sonicated as-prepared nanorods for 1 h, yielding $CaWO_4$ and $Ba_{0.5}Sr_{0.5}WO_4$ nanostructures (Figures S7A and S7C) possessing length distributions of 0.83 ± 0.12 and 0.89 ± 0.27 μm, respectively, but were unable to clearly differentiate their optical behavior from that of untreated nanorods (Figures S7B and S7D). It has been previously reported that in some systems, such as ZnO and $PbCrO_4$, PL intensities are susceptible to and will actually increase with increasing nanorod length,[72,73] presumably due to the lessening influence of defects as the nanorods become longer. We did not observe such an effect herein.

Moreover, we performed additional experiments, coating our nanorods with organic ligands, such as either PAA or oleic acid, to determine potential surface effects on optical behavior. Figure S8 contains IR spectroscopy data associated with functional groups present on the surfaces of functionalized $CaWO_4$ nanorods. In Figure S8A, for PAA-coated nanorods, the bands at 1230 and 1450 cm^{-1} can be assigned to the antisymmetric and symmetric vibrational modes of the $-COO^-$ group. The band at 1700 cm^{-1} is associated with the stretching mode of the $-COOH$ group. Additionally, the shoulder at 2920 cm^{-1} can be ascribed to the asymmetric stretching mode of $-CH_3$ groups. On the basis of these observations, one can conclude that PAA is bound to the surface of $CaWO_4$ nanorods. In oleic acid-coated nanorods, the band at 2916 cm^{-1} in Figure S8B is significantly enhanced, suggesting an increase in quantity of $-CH_3$ groups. All of the remaining bands also suggest adsorption of oleic acid onto the nanorod surface through formation of bidentate bonds.[74,75] While our data showed that such surfactant capping could definitely yield a more stable dispersion of functionalized nanorods, on the order of days as compared with merely hours for as-prepared nanorods, in aqueous solvents, in agreement with a previous report,[76]

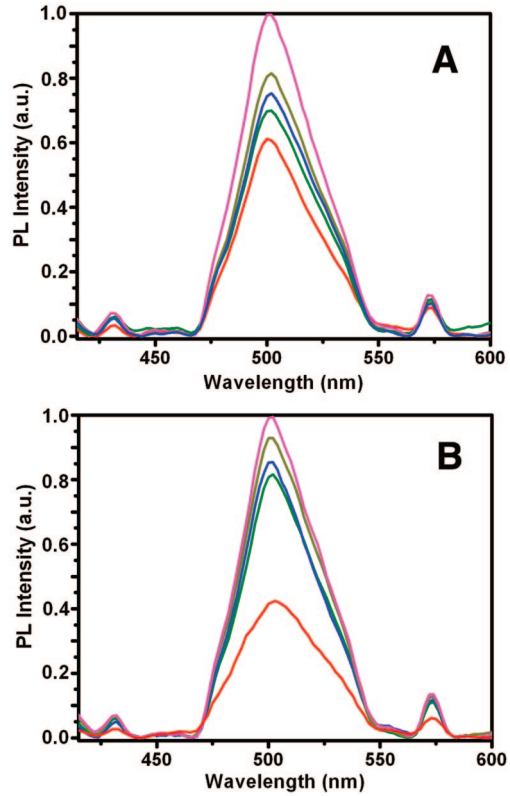

Figure 11. Photoluminescence spectra of as-prepared alkaline-earth-metal tungstate solid−solution nanorods collected at room temperature: (A) $Sr_{1-x}Ca_xWO_4$ nanorods. From top to bottom: $CaWO_4$ (pink), $Sr_{0.3}Ca_{0.7}WO_4$ (olive green), $Sr_{0.5}Ca_{0.5}WO_4$ (blue), $Sr_{0.7}Ca_{0.3}WO_4$ (dark green), and $SrWO_4$ (red), respectively. (B) $Ba_{1-x}Sr_xWO_4$ nanorods. From top to bottom: $SrWO_4$ (pink), $Ba_{0.3}Sr_{0.7}WO_4$ (olive green), $Ba_{0.5}Sr_{0.5}WO_4$ (blue), $Ba_{0.7}Sr_{0.3}WO_4$ (dark green), and $BaWO_4$ (red).

PL behavior for our processed tungstate nanorods, though slightly different, was indistinguishable within the limits of experimental error from that of uncapped nanorods (Figure S9). By contrast, in general, the presence of capping agents such as either polymer or alkyl amines has been known to either enhance or quench photoluminescence relative to that of the corresponding, unmodified nanorods.[70,77–79]

Figure 11A illustrates typical PL spectra of $Sr_{1-x}Ca_xWO_4$ nanorods, where $x = 1$, 0.7, 0.5, 0.3, and 0, with increasing Sr content from top to bottom. It can be observed that all five emission curves exhibit a broad luminescence in the blue wavelength range and possess a triple-peak, spread-eagle-shape structure wherein a relatively narrow central peak is surrounded by two shoulders.[68,71,80] Similar behavior was observed in the collective emission spectra of nanorods of the $Ba_{1-x}Sr_xWO_4$ system (Figure 11B).

For all samples, all of the emission peak positions were not noticeably altered by the variation in chemical composition,[31] implying that the energy gap related to the blue emission was not overly affected by changes in either Ca, Sr, or Ba content. As mentioned, the dominant blue emission

(65) Ling, Z. C.; Xia, H. R.; Ran, D. G.; Liu, F. Q.; Sun, S. Q.; Fan, J. D.; Zhang, H. J.; Wang, J. Y.; Yu, L. L. *Chem. Phys. Lett.* **2006**, *426*, 85.
(66) Zhang, G.; Jia, R.; Wu, Q. *Mater. Sci. Eng., B* **2006**, *128*, 254.
(67) Tarte, P.; Liegeois-Duyckaerts, N. *Spectrochim. Acta, Part A* **1972**, *28*, 2029.
(68) Ryu, J. H.; Yoon, J.-W.; Shim, K. B. *Electrochem. Solid-State. Lett.* **2005**, *8*, D15.
(69) Orhan, E.; Anicete-Santos, M.; Maurera, M. A. M. A.; Pontes, F. M.; Paiva-Santos, C. O.; Souza, A. G.; Varela, J. A.; Pizani, P. S.; Longo, E. *Chem. Phys.* **2005**, *312*, 1.
(70) Oaki, Y.; Imai, H. *Adv. Mater.* **2006**, *18*, 1807.
(71) Nikl, M.; Bohacek, P.; Mihokova, E.; Kobayashi, M.; Ishii, M.; Usuki, Y.; Babin, V.; Stolovich, A.; Zazubovich, S.; Bacci, M. *J. Lumin.* **2000**, *87−89*, 1136.
(72) Al-Suleiman, M.; Che Mofor, A.; El-Shaer, A.; Bakin, A.; Wehmann, H.-H.; Waag, A. *Appl. Phys. Lett.* **2006**, *89*, 231911.
(73) Cheng, B.; Guo, H.; Yu, J.; Zhao, X. *J. Alloys Compd.* **2007**, *431*, L4.
(74) Willis, A. L.; Turro, N. J.; O'Brien, S. *Chem. Mater.* **2005**, *17*, 5970.
(75) Zhang, T.; Ge, J.; Hu, Y.; Yin, Y. *Nano Lett.* **2007**, *7*, 3203.
(76) Wang, L.; Li, Y. *Nano Lett.* **2006**, *6*, 1645.
(77) Zhang, Q.; Russell, T. P.; Emrick, T. *Chem. Mater.* **2007**, *19*, 3712.
(78) Zhang, Y.; Guo, J.; White, T.; Tan, T. T. Y.; Xu, R. *J. Phys. Chem. C* **2007**, *111*, 7893.
(79) Lu, S. W.; Lee, B. I.; Wang, Z. L.; Tong, W.; Wagner, B. K.; Park, W.; Summers, C. J. *J. Lumin.* **2001**, *92*, 73.
(80) Polak, K.; Nikl, M.; Nitsch, K.; Kobayashi, M.; Ishii, M.; Usuki, Y.; Jarolimek, O. *J. Lumin.* **1997**, *72−74*, 781.

band of the metal tungstates can be attributed to charge-transfer transitions within the $[WO_4^{2-}]$ group between the last fully occupied t_1 orbital and the first empty 2e orbital.[81] That is, excitation from the ground state ($^1A_1$) of $[WO_4^{2-}]$ gives rise to four excited states, i.e., $^1T_2$, $^1T_1$, $^3T_2$, and $^3T_1$, from which only the transition between $^1A_1$ and $^1T_2$ is electric dipole allowed.[82] However, the WO_4^{2-} complexes in scheelite tungstates are slightly distorted from T_d to D_{2d} symmetry by the influence of the Jahn−Teller effect (through coupling of Jahn−Teller active vibrational modes of t_2 symmetry for instance) and electron−phonon interactions in general.[80,83] Hence, the orbitally degenerate T state undergoes distortion and symmetry lowering to a D_{2d} symmetry state, which strongly enhances the number of transitions observed. Specifically, both $^1A_1$ to $^1T_2$, $^1T_1$ as well as $^1A_1$ to $^3T_2$, $^3T_1$ transitions become partially allowable, thereby rendering radiative transitions from low-lying triplet excited states to the $^1A_1$ ground state as clearly detectable emission peaks (i.e., at 437 nm) in the blue luminescent spectra. The resulting theoretical emission bands therefore possess a spread-eagle shape.[84] In addition, the presence of weak green and red emission bands in our nominally pure nanorods could be ascribed to the presence of radiative transitions within defect centers, such as Frenkel defects (i.e., oxygen ions shifted to intersite positions with a simultaneous creation of a vacancy) on the surfaces of our samples as well as the possibility of Schottky defects, i.e., WO_3.[68,81,82]

It is worth emphasizing that though emission peak positions were essentially unchanged across sample composition, variations in emission peak intensities were observed. Photoluminescence is sensitive to local lattice symmetry and could be used as an intrinsic probe to map out variations in scheelite nanocrystals, characteristic of changes in chemical composition, such as in lattice dimension and symmetry which often accompany size reductions.[7] We indeed found this to be the case with our samples.

In Figure 11A, Ca-rich nanorods showed a very strong luminescence, whereas Sr-rich nanorods evinced a much weaker emission. To account for the inefficiency of luminescence with increasing Sr content, it has been suggested that because Sr^{2+} ions (1.13 Å), surrounding the tungstate groups, are bigger than Ca^{2+} ions (0.99 Å), they do not effectively counteract the expansion of the WO_4^{2-} complexes upon excitation as well as Ca^{2+} ions do. As a result, there is a lower thermal quenching temperature of the blue luminescence with increasing Sr content and a correspondingly higher probability of radiationless transitions.[85] By contrast, in Figure 11B, Sr-rich nanorods yielded a comparatively stronger luminescence than their Ba-rich nanorod counterparts. An analogous argument could be made with respect to the size of the larger Ba^{2+} ions (1.35 Å) relative to Sr^{2+} ions (1.13 Å), rendering them less capable of counteracting the expansion of WO_4^{2-} groups upon excitation and thereby indirectly contributing to an increase in competing radiationless transitions.[32]

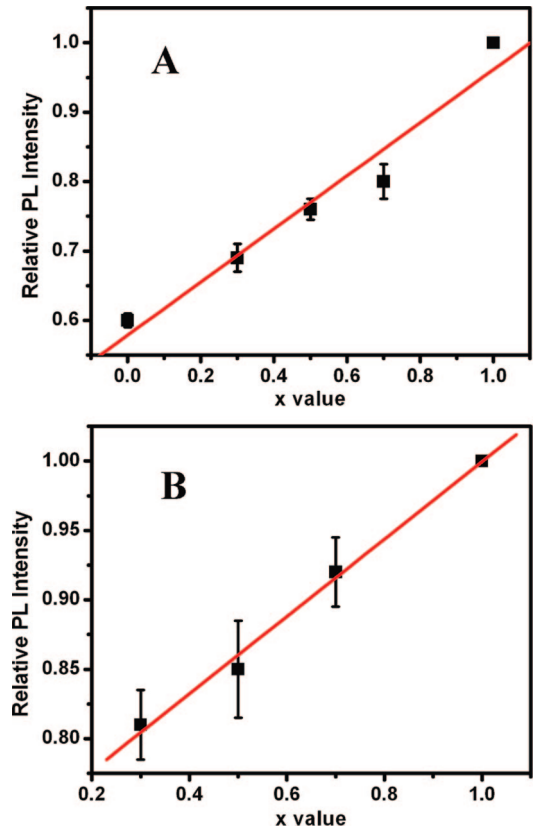

Figure 12. Dependence of normalized photoluminescence intensities on the rationally modulated chemical compositions of as-prepared (A) $Sr_{1-x}Ca_xWO_4$ and (B) $Ba_{1-x}Sr_xWO_4$ solid−solution nanorods.

Importantly, it should be noted that with decreasing values of x and hence decreasing Ca content in the $Sr_{1-x}Ca_xWO_4$ system, the normalized intensities of the major emission peaks decreased in parallel in a systematic fashion, from 100%, 80%, 76%, 69%, and to 60%, associated with values of $x = 1$, 0.7, 0.5, 0.3, and 0. Figure 12A highlights a linear relationship between the solid−solution composition-dependent **x** values and the corresponding normalized PL intensities (**y**), as described by eq 5, with a slope of 0.38 ($R^2 = 0.953$).

$$\mathbf{y} = 0.38(\mathbf{x}) + 0.58 \quad (5)$$

We found an analogous relationship between the normalized PL intensity and the chemical composition in the $Ba_{1-x}Sr_xWO_4$ system. That is, with decreasing values of x and hence vanishing Sr content, the normalized intensities of the major emission peaks similarly but predictably decreased from 100%, 92%, 85%, 81%, to 41%, associated with $SrWO_4$, $Sr_{0.7}Ba_{0.3}WO_4$, $Sr_{0.5}Ba_{0.5}WO_4$, $Sr_{0.3}Ba_{0.7}WO_4$, and $BaWO_4$, respectively. However, as others have observed the luminescence of pure $BaWO_4$ crystals and films to be anomalously weak and potentially less interpretable as compared with that of their $SrWO_4$ analogues,[70,32] we only considered data corresponding to $x = 1$, 0.7, 0.5, and 0.3 in the $Ba_{1-x}Sr_xWO_4$ system in our subsequent analysis. Figure 12B therefore illustrates a linear relationship between the solid−solution composition-dependent **x** values and the corresponding normalized PL intensities (**y**), as described by eq 6, with a slope of 0.28 ($R^2 = 0.994$).

(81) Grasser, R.; Scharmann, A. *J. Lumin.* **1976**, *12/13*, 473.
(82) Grasser, R.; Scharmann, A.; Strack, K.-R. *J. Lumin.* **1982**, *27*, 263.
(83) Nike, M.; Bohacek, P.; Mihokove, E.; Kobayashi, M.; Ishii, M.; Usuki, Y.; Babin, V.; Stolovich, A.; Zazubovich, S.; Bacci, M. *J. Lumin.* **2000**, 87−89.
(84) Toyozawa, Y.; Inoue, M. *J. Phys. Soc. Jpn.* **1966**, *21*, 1663.
(85) Cho, W.-S.; Yoshimura, M. *J. Appl. Phys.* **1998**, *83*, 518.

$$\mathbf{y} = 0.28(\mathbf{x}) + 0.72 \quad (6)$$

Apart from a controlled use of small percentages of dopants and guest ion intercalants,[86] a clear dependence of photoluminescence intensity on chemical composition has rarely been convincingly demonstrated. Nonetheless, this effect, though, has been previously detected in $CuGaSe_2$ films.[87,88] In addition, optical properties, including absorption and PL, have been systematically tuned in compositionally modulated $Zn_xCd_{1-x}S$ alloyed nanocrystals, $Zn_xCd_{1-x}Te$ alloyed nanocrystals, as well as binary and ternary mercury chalcogenide clusters.[89–91] Moreover, the photoluminescence quantum yield of CdTe quantum dots has been found to depend on the precise stoichiometric ratio of Cd to Te precursors used.[92] However, a clear correlation between the chemical composition of robust nanoscale solid solutions and photoluminescent intensity, as established herein, has, to the best of our knowledge, never been observed in 1D metal oxide systems. As such, this finding reported herein is highly significant from the point of view of obtaining predictive structure−property relationships in 1D nanorods prepared from solid solutions. Specifically, in our case, using a quasi-standardization plot, we can readily compute the magnitude of expected PL intensities from a knowledge of the precise chemistry of well-defined alkaline-earth-metal tungstate solid solution samples, whereas, conversely, PL data can be reliably used to deduce the exact chemical compositions of these nanoscale materials.

Time-resolved luminescence measurements were carried out in order to further explore the photoluminescent properties of our solid−solution nanorod samples. Figure S10 shows a typical time-resolved luminescence decay curve of as-prepared $SrWO_4$ nanorods, which can be satisfactorily fitted into a single-exponential function with the decay lifetime, τ, equal to 1.62 ± 0.05 μs. Additional lifetime data with appropriate standard deviations for all of our samples are listed in Table 1. Within our experimental resolution, there does not seem to be an obvious trend with respect to photoluminescent lifetimes across samples of different cation stoichiometry (Ca, Sr, Ba). The average lifetime was calculated to be 1.6 ± 0.1 μs, which is comparable to the reported value of bulk $CaWO_4$ crystal which is on the order of microseconds.[93,94] In addition, any real differences in the decay constants may be attributed to corresponding differences in excitation conditions.[95] The exponential tail of the decay curve reflects the lifetime of the exciton emission due to radiative recombination of photoinduced charge carriers.[96,97] In general, the presence of surface defects (e.g., vacancy centers) as well as surface degradation and disorder may decrease observed lifetimes, whereas compositional disorder and exciton localization may have the opposite effect and increase lifetimes.[92,98] The fact that essentially similar lifetimes were observed for all systems implies that the surface properties of our nanorods associated with these luminescence processes were effectively identical for each sample.

Table 1. Emission Lifetimes Measured at Room Temperature, Under Ambient Conditions, at 502 nm for As-Prepared Alkaline-Earth-Metal Tungstate Solid−Solution Nanorods

sample	lifetime (μs)	standard deviation (μs)
$CaWO_4$	1.64	0.06
$Sr_{0.3}Ca_{0.7}WO_4$	1.67	0.07
$Sr_{0.5}Ca_{0.5}WO_4$	1.84	0.10
$Sr_{0.7}Ca_{0.3}WO_4$	1.47	0.04
$SrWO_4$	1.62	0.05
$Ba_{0.3}Sr_{0.7}WO_4$	1.71	0.07
$Ba_{0.5}Sr_{0.5}WO_4$	1.41	0.03
$Ba_{0.7}Sr_{0.3}WO_4$	1.54	0.06
$BaWO_4$	1.47	0.02

While we were not able to measure the quantum yield (QY) directly, we can estimate it by comparing our measured lifetimes to those reported in the literature using eq 7

$$QY_A = \frac{\frac{1}{\tau_r}}{\frac{1}{\tau_r} + \frac{1}{\tau_{nr}^A}}; \frac{QY_A}{QY_B} = \frac{\left(\frac{1}{\tau_r} + \frac{1}{\tau_{nr}^B}\right)}{\left(\frac{1}{\tau_r} + \frac{1}{\tau_{nr}^A}\right)} \quad (7)$$

where A represents our nanorod systems and B is associated with the bulk reference. τ_r and τ_{nr} represent the radiative and nonradiative lifetimes, respectively.

For example, one study quotes a lifetime ranging from 5 to 6.7 μs at room temperature,[93] which suggests a corresponding quantum efficiency value of ~24−32% relative to bulk calcium tungstate material. It should be noted that in that bulk study, the reported lifetime values were not representative of the true radiative lifetime of the material since the room-temperature efficiency was arbitrarily set to 1. As such, we should emphasize that the computed quantum yield of 24−32% for our nanorods cannot necessarily be considered as an absolute quantum yield. A further confirmation of this assertion can be found in another paper, reporting a low-temperature (75 K) decay time of >200 μs;[11] using 200 μs in our calculations would have reduced our quantum yield to less than 1%. On the basis of all of this data, it is reasonable to state that the quantum yield of our as-prepared alkaline-earth-metal tungstate nanorods is likely to be no worse than 25% as compared with their bulk counterparts at room temperature. We expect to continue with additional comprehensive photooptical studies on these as well as

(86) Park, T.-R.; Lee, S.; Holtz, M.; Solin, S. A. *Phys. Rev. B* **1995**, *51*, 17925.
(87) Siebentritt, S.; Schuler, S. *J. Phys. Chem. Solids* **2003**, *64*, 1621.
(88) Xue, C.; Papadimitriou, D.; Esser, N. *J. Phys. D: Appl. Phys.* **2004**, *37*, 2267.
(89) Kuno, M.; Higginson, K. A.; Qadri, S. B.; Yousuf, M.; Lee, S. H.; Davis, B. L.; Mattoussi, H. *J. Phys. Chem. B* **2003**, *107*, 5758.
(90) Li, Y.; Ye, M.; Yang, C.; Li, X.; Li, Y. *Adv. Funct. Mater.* **2005**, *15*, 433.
(91) Wang, Y.; Hou, Y.; Tang, A.; Feng, B.; Li, Y.; Liu, J.; Teng, F. *J. Cryst. Growth* **2007**, *308*, 19.
(92) Zhao, K.; Li, J.; Wang, H.; Zhuang, J.; Yang, W. *J. Phys. Chem. C* **2007**, *111*, 5618.
(93) Beard, G. B.; Kelly, W. H.; Mallory, M. L. *J. Appl. Phys.* **1962**, *33*, 144.
(94) Born, G.; Hofstaetter, A.; Scharmann, A.; Schwarz, G. *J. Lumin.* **1970**, *1/2*, 641.
(95) Mikhailik, V. B.; Kraus, H.; Wahl, D.; Itoh, M.; Koike, M.; Bailiff, I. K. *Phys. Rev. B* **2004**, *69*, 205110.
(96) de Mello Donegá, C.; Hickey, S. G.; Wuister, S. F.; Vanmaekelbergh, D.; Meijerink, A. *J. Phys. Chem. B* **2003**, *107*, 489.
(97) Lee, H.; Holloway, P. H.; Yang, H.; Hardison, L.; Kleiman, V. D. *J. Chem. Phys.* **2006**, *125*, 164711.
(98) Wehrenberg, B. L.; Wang, C.; Guyot-Sionnest, P. *J. Phys. Chem. B* **2002**, *106*, 10634.

analogous systems since there are few such studies in the literature that conclusively deal with these important issues.

Conclusions

The current report demonstrates the ambient, room-temperature synthesis using a modified template-directed methodology of single-crystalline alkaline-earth-metal tungstates AWO_4 (A = Ca, Sr, Ba) nanorods as well as the corresponding series of their crystalline solid−solution analogues, $Sr_{1-x}Ca_xWO_4$ and $Ba_{1-x}Sr_xWO_4$ ($0 < x < 1$), with varying controllable sizes. As-obtained photoluminescent lifetimes and quantum yields suggest that these nanoscale materials are comparable in optical behavior to those of bulk. The growth mechanism for these 1D nanostructures has been previously discussed.[60,61] The point is that the pores of the polycarbonate templates provide for a spatially constraining but robust environment in which to control pure, single-crystalline nanorod preparation.

The resulting nanorods have been extensively characterized via microscopy and spectroscopy. Because of the simplicity and versatility of the approach used, it is anticipated that we can generalize this methodology to the preparation of other important classes of stoichiometrically precise nanomaterials with controllable size and shape. In addition, whereas much of the relevant literature in solid−solution synthesis has focused on generating 1D nanostructures of bimetallic materials, such as diluted magnetic, semiconducting (DMS) nanorods in particular,[99–103] the current work is focused on an important extension of this idea to trimetallic oxide systems. In fact, the relatively mild synthetic methodology we developed offers improved control over morphology, tunable chemical composition, and a reliable understanding of associated physical properties. Moreover, the composition-modulated luminescence properties over several distinctive series of as-prepared solid−solution nanorods of alkaline-earth-metal tungstates provide the fundamental basis for a more thorough investigation and understanding of their optical and optoelectronic properties, which may eventually lead to the rational incorporation of these materials into functional nanoscale devices.

Acknowledgment. We acknowledge the U.S. Department of Energy (DE-AC02-98CH10886) for facility and personnel support. Lifetime data were collected using instrumentation located at the Center for Functional Nanomaterials at Brookhaven National Laboratory. D. Hirt (Materials Research Laboratories, Inc.) is acknowledged for his work with the XPS measurements. We also thank the National Science Foundation (CAREER Award DMR-0348239) and the Alfred P. Sloan Foundation (2006−2008) for PI support and experimental supplies. Moreover, we are grateful to D. Wang (Boston College) as well as to H. Zhou, S. van Horn, and J. Quinn (SUNY Stony Brook) for their assistance with electron microscopy.

Supporting Information Available: Additional figures (PDF). This material is available free of charge via the Internet at http://pubs.acs.org.

CM800011J

(99) Zhang, X. L.; Qiao, R.; Qiu, R.; Li, Y.; Kang, Y. S. *J. Phys. Chem. A* **2007**, *111*, 4195.
(100) Jun, Y.-W.; Jung, Y.-Y.; Cheon, J. *J. Am. Chem. Soc.* **2002**, *124*, 615.
(101) Na, C. W.; Han, D. S.; Kim, D. S.; Kang, Y. J.; Lee, J. Y.; Park, J.; Oh, D. K.; Kim, K. S.; Kim, D. *J. Phys. Chem. B* **2006**, *110*, 6699.
(102) Ando, K. *Science* **2006**, *312*, 1883.
(103) Zhang, Y. C.; Chen, W. W.; Hu, X. Y. *Cryst. Growth Des.* **2007**, *7*, 580.